

Dynamical crystallization in a low-dimensional Rydberg gas

Peter Schauß^{1,*}, Johannes Zeiher¹, Takeshi Fukuhara¹, Sebastian Hild¹, Marc Cheneau², Tommaso Macrì³, Thomas Pohl³, Immanuel Bloch^{1,4}, and Christian Gross¹

¹Max-Planck-Institut für Quantenoptik, 85748 Garching, Germany

²Laboratoire Charles Fabry, Institut d'optique Graduate School - CNRS - Université Paris Sud, 91127 Palaiseau, France

³Max-Planck-Institut für Physik komplexer Systeme, 01187 Dresden, Germany and

⁴Ludwig-Maximilians-Universität, Fakultät für Physik, 80799 München, Germany

(Dated: 3 April 2014)

Dominating finite-range interactions in many-body systems can lead to intriguing self-ordered phases of matter. Well known examples are crystalline solids or Coulomb crystals in ion traps. In those systems, crystallization proceeds via a classical transition, driven by thermal fluctuations. In contrast, ensembles of ultracold atoms laser-excited to Rydberg states provide a well-controlled quantum system [1], in which a crystalline phase transition governed by quantum fluctuations can be explored [2–4]. Here we report on the experimental preparation of the crystalline states in such a Rydberg many-body system. Fast coherent control on the many-body level is achieved via numerically optimized laser excitation pulses [2–4]. We observe an excitation-number staircase [2–7] as a function of the system size and show directly the emergence of incompressible ordered states on its steps. Our results demonstrate the applicability of quantum optical control techniques in strongly interacting systems, paving the way towards the investigation of novel quantum phases in long-range interacting quantum systems, as well as for detailed studies of their coherence and correlation properties [2–8].

Rydberg atoms exhibit unique properties that are key to realize and explore novel quantum many-body Hamiltonians and their phases. The strong van der Waals interaction between them allows to create many-body systems with tailored long-range interactions in neutral ultra-cold atom samples [1, 9, 10]. Complete experimental control of these systems is possible using the well developed toolbox of quantum optics for the laser-excitation to the Rydberg states. The magnitude of the resulting interactions between the Rydberg atoms is determined by the choice of the excited state and it can exceed all other relevant energy scales on distances of several microns, thereby leading to an ensemble dominated by long-range interactions. In this regime, the ground state of the resulting many-body system is expected to show crystalline ordering of the Rydberg excitations, which can be understood in the limit of vanishing coupling as the classical closest packing of hard spheres [11]. The lattice constant of the crystal is set by the dipole blockade radius R_b [12, 13], defined as the inter-particle spacing at which the dipole interaction between two Rydberg atoms exceeds the spectral range of the optical coupling. To prepare the system in this crystalline phase, a dynamical approach has been suggested that adiabatically connects the ground state containing no Rydberg excitations with the targeted crystalline state. At the heart of this *dynamical crystallization* technique is the coherent control of the many-body system [2–4, 14–17].

Previous experiments showed direct or indirect evidence for correlations caused by the long-range interac-

tions in Rydberg many-body systems, such as a universal scaling of the Rydberg excitation number [18], sub-Poissonian counting statistics [17, 19, 20], photon correlations [21, 22], characteristic exciton dynamics [23] or spatial ordering of the excitations [24–26]. However, all measurements have predominantly probed features of excited many-body states that – next to the ground state – are also strongly influenced by the dramatically enhanced interaction scales.

Here, we report on the deterministic preparation of crystalline many-body states in small Rydberg systems via coherently controlled excitation as proposed in refs. [2–4]. For one-dimensional systems we experimentally realize the dipole-blockade staircase and demonstrate the emergence of crystalline states with a vanishing compressibility. We trace the evolution of the quantum state during the dynamic preparation by spatially resolved detection of the excitations at successive times. Additionally, we developed a novel technique to control the initial atomic density distribution (Methods). This has turned out to be a crucial requirement to observe low energy states, especially for small two-dimensional systems where the many-body energy spectrum is significantly denser than in the one-dimensional case and strongly depends on the initial shape. In such two-dimensional systems we observe a sharp concentration of the Rydberg excitations along the edge of the initial cloud, which is expected for the energetically low lying many-body states.

The physical system studied here is a well-defined linear or disc-shaped atomic sample in an optical lattice with one atom per site. The rubidium-87 atoms are coupled to the Rydberg state $43S_{1/2}$ with a controlled time-dependent Rabi frequency $\Omega(t)$ and detuning $\Delta(t)$. The corresponding theoretical model describing this system is

* Electronic address: peter.schauss@mpq.mpg.de

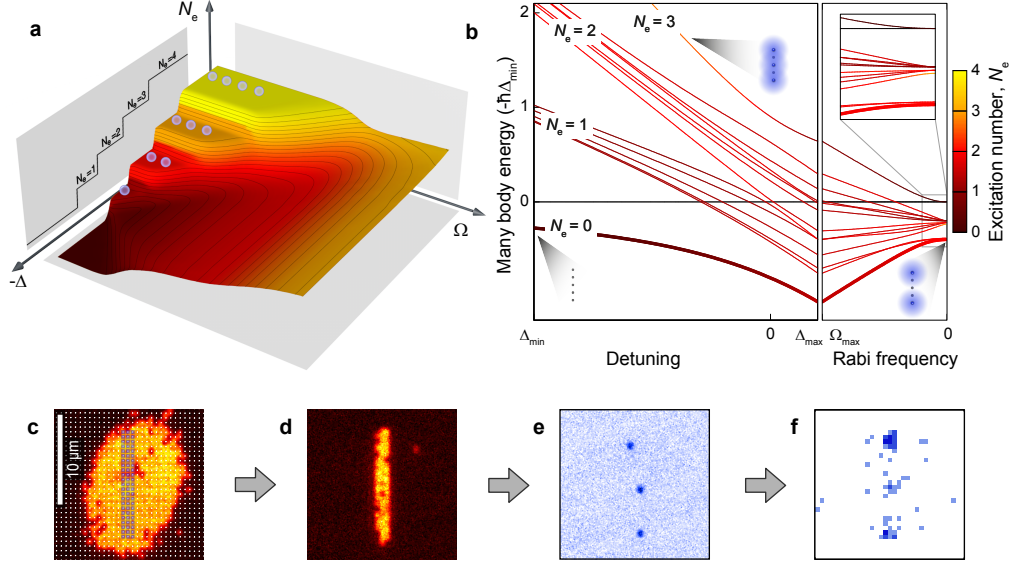


Figure 1. **Schematic illustrating the phase diagram, energy spectrum and experimental sequence.** **a**, Schematic phase diagram. The colour scale indicates the number of Rydberg excitations in the many-body ground state of a one-dimensional system. The number of Rydberg excitations N_e is visualized in the crystalline phase by the small spheres. For illustration, the detuning Δ and Rabi frequency Ω axes are rescaled by their sixth root. **b**, Schematic illustrating the evolution of the excitation spectrum during a sweep, where coupling strength $\Omega(t)$ and detuning $\Delta(t)$ are controlled. The spectrum was calculated for an exemplary 1D system of five atoms. First, the detuning is changed from Δ_{\min} to Δ_{\max} at constant Rabi frequency Ω_{\max} , with Δ_{\max} chosen to prepare $N_e = 2$ Rydberg excitations. Subsequently, the Rabi frequency is reduced from Ω_{\max} to 0. The inset is a zoom into the end of the sweep highlighting the shrinking gap between the energy levels. The colour of each line indicates the mean number of Rydberg excitations in the many-body state. For strongly negative detuning the four different manifolds correspond to the excitation number Fock states, whose occupation N_e is indicated in the figure. In three limiting cases in which the states become classical the spatial excitation pattern is shown (blue circles: Rydberg atoms, grey circles: ground state atoms). **c-e**, Exemplary fluorescence pictures from different times in the experimental cycle. **c**, Mott insulator with lattice sites (white dots) and spatial light modulator pattern (semi-transparent overlay). **d**, Initial atom configuration, **e**, Single shot Rydberg excitation pattern. **f**, Rydberg excitation density after averaging 40 experimental runs (darker colour means more detected atoms).

the so-called "frozen Rydberg gas" Hamiltonian, in which only the internal electronic degrees of freedom are considered. This is justified by the short time scale on which our experiments take place during which the motion of

the atoms in the lattice is negligible [27, 28]. Adopting a two-level description, the many-body dynamics of the internal atomic states is governed by the Hamiltonian

$$\hat{H} = \frac{\hbar\Omega(t)}{2} \sum_{\mathbf{i}} \left(|e^{(\mathbf{i})}\rangle\langle g^{(\mathbf{i})}| + |g^{(\mathbf{i})}\rangle\langle e^{(\mathbf{i})}| \right) + \sum_{\mathbf{i} \neq \mathbf{j}} \frac{V_{\mathbf{ij}}}{2} \hat{n}_e^{(\mathbf{i})} \hat{n}_e^{(\mathbf{j})} - \hbar\Delta(t) \sum_{\mathbf{i}} \hat{n}_e^{(\mathbf{i})}. \quad (1)$$

Here, the vectors $\mathbf{i} = (i_x, i_y)$ label the position of the atoms on the lattice. The operators $|e^{(\mathbf{i})}\rangle\langle g^{(\mathbf{i})}|$ and $|g^{(\mathbf{i})}\rangle\langle e^{(\mathbf{i})}|$ describe the transition from the ground state $|g\rangle$ to the Rydberg state $|e\rangle$, while the operator $\hat{n}_e^{(\mathbf{i})} = |e^{(\mathbf{i})}\rangle\langle e^{(\mathbf{i})}|$ represents the Rydberg state occupation on site (\mathbf{i}) . The first term of the Hamiltonian describes the coherent coupling between ground and excited state with the time-dependent Rabi frequency $\Omega(t)$. The second

term arises due to the van der Waals interaction between two atoms in the Rydberg state. For the $43S_{1/2}$ state of rubidium-87 $V_{\mathbf{ij}} = -C_6/r_{\mathbf{ij}}^6$ is repulsive due to a negative van der Waals coefficient $C_6 < 0$. Here, $r_{\mathbf{ij}} = a_{\text{lat}}|\mathbf{i} - \mathbf{j}|$ is the distance between two atoms on the lattice with period a_{lat} . The last term corresponds to an effective chemical potential for the Rydberg excitations that can be controlled by the detuning $\Delta(t)$.

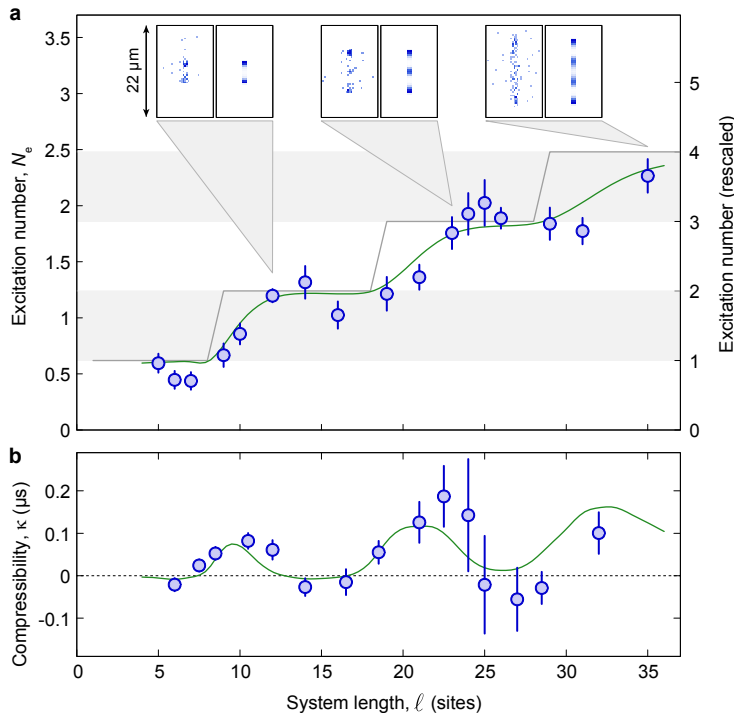


Figure 2. Identification of the crystalline phase. **a**, Excitation number versus system length for a one-dimensional system. Blue circles correspond to the experimental mean number of Rydberg excitations N_e after the optimized sweep. The right axis shows the excitation number corrected for the detection efficiency. The green line is the result of the numerical simulation for the experimental initial states, taking into account an initial state filling of 0.8 and length fluctuations of the order of one site. The grey line shows the classical ($\Omega = 0$) prediction. Insets: Measured spatial distribution of Rydberg excitations (left) and corresponding theory (right) for system lengths ℓ of 12, 23 and 35 sites. The brightness (light to dark) translates to the normalized number of excitations. **b**, Compressibility κ of the prepared states. Blue circles are derived from the experimental data shown in **a** using a numerical derivative. The green line is a direct numerical result (Methods). All error bars s.e.m.

Rydberg atoms have recently been discussed as a platform for the simulation of quantum magnetism. Especially, the frozen gas Hamiltonian has been at the focus of theoretical and experimental interest due to its rich variety of strongly-correlated phases [5–7]. Introducing spin-1/2 operators, the Hamiltonian can be rewritten in the form of an Ising model with long-range spin interactions in an effective transverse ($\hbar\Omega$) and longitudinal ($-\hbar\Delta$) magnetic field [6, 8]. In the classical limit, $\Omega = 0$ and for $\Delta > 0$, the many-body ground state corresponds to crystalline Fock states with a total excitation number $N_e = \langle \hat{N}_e \rangle = \sum_i \langle \hat{n}_e^{(i)} \rangle$. Consequently, the Rydberg excitation number N_e forms a complete devil’s staircase [29] as a function of Δ in the thermodynamic limit. In a one-dimensional chain of $\ell \gg N_e$ lattice sites, the excitation number increases from N_e to $N_e + 1$ at the critical detunings $\ell^6 \hbar \Delta_c \approx 7|C_6|N_e^6/a_{\text{lat}}^6$ separating successive crystal states with a lattice spacing $a_{\text{lat}}\ell/(N_e - 1)$ [2]. The laser coupling introduces quantum fluctuations, whose effect has been studied in a number of recent theory works [5–8, 30]. Upon increasing Ω , it has been predicted that, in the thermodynamic limit, the system undergoes a two-stage quantum melting [6, 7] via an incommensurate floating solid with algebraic correlations followed by a Kosterlitz-Thouless transition [6, 7] to a disordered phase. The corresponding scenario for a finite lattice is shown schematically in Fig. 1a. While finite size effects naturally broaden the transitions in the (Ω, Δ) parameter space, extended lobes corresponding to crystalline states of N_e excitations with vanishing number fluctuations can be well identified for typical parameters of our experi-

ments.

The preparation of the crystalline states requires a fast dynamical control due to the short lifetime of the Rydberg states of typically several tens of microseconds. Our initial state with all atoms in their electronic ground state coincides with the many-body ground state of the system for negative detunings and $\Omega = 0$. Since for small coupling strength Ω the energy gap to the first excited state closes at the transition points Δ_c between successive N_e -manifolds, Ω and Δ have to be varied simultaneously in order to maximize the adiabaticity of the preparation scheme. An intuitive and simple choice of the path $(\Omega(t), \Delta(t))$ starts with a large negative detuning Δ_{min} at which the coupling Ω is switched on [2–4]. Next, the detuning is increased to the desired final blue-detuned value $\Delta_{\text{max}} > 0$, followed by a gradual reduction of the coupling strength Ω to zero. In the final stage of this last step the energy of several many-body states becomes nearly degenerate, as illustrated in Fig. 1b for an exemplary system of five excitations. These lowest many-body excited states all belong to the same N_e -manifold but feature a finite density of dislocations with respect to the perfectly ordered classical ground state. In practice this leads to unavoidable non-adiabatic transitions at the end of the laser pulse, resulting in non-classical crystalline states composed of spatially localized collective excitations [2].

Our experiment started from a two-dimensional degenerate gas of approximately 250 to 700 rubidium-87 atoms confined to a single antinode of a vertical (z -axis) optical lattice. The gas was driven deep into the Mott-insulating phase by adiabatically turning on a square optical lat-

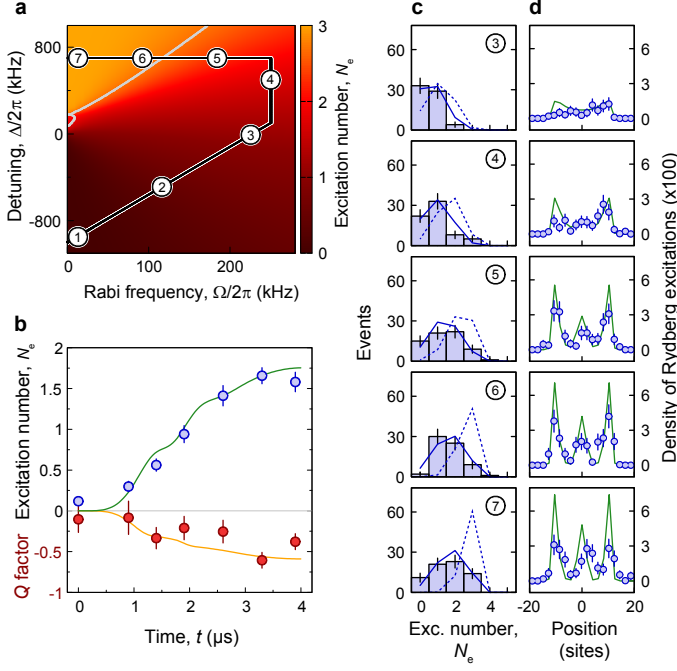


Figure 3. Dynamical crystallization. **a**, Illustration of the laser sweep. The black line shows the path of the sweep through the phase diagram, the numbered positions mark the measurements (c.f. **c**). The grey line indicates the boundary of the crystalline lobes, where the Q factor drops below -0.9 . The phase diagram was calculated for the experimental parameters. **b**, Mean number of Rydberg excitations (blue circles) and Q factor (red circles) for the seven times marked in **a** together with the theoretical prediction. **c**, Experimental and theoretical probability distributions of the number of Rydberg excitations along the sweep (c.f. **a**). Blue boxes show experimental data and the dashed and solid lines represent the theoretical result for detection efficiencies of $\alpha = 1$ and $\alpha = 0.62$, respectively. **d**, Transversally averaged distributions (probability per site) of the excitations for the same times as in **c** with a binning of two sites (blue circles). The slight asymmetry towards the right might be due to a gradient in the Rabi frequency (Methods). The green line is the numerical result. All error bars s.e.m.

tice with period $a_{\text{lat}} = 532 \text{ nm}$ in the xy -plane [31]. We used a deconfining beam to reduce the harmonic potential induced by the lattice beams and thereby enlarged the spatial extension of a single occupancy Mott insulating state [32]. Next, we prepared the initial atomic density distribution precisely by cutting out the desired cloud shape from the initial Mott insulator using a spatial light modulator (Fig. 1c-d and Methods). For our measurements we chose line- or disc-shaped atomic samples of well controlled length or radius. The line had a width of three lattice sites and a variable length ℓ . Since this width was much smaller than the blockade radius of approximately nine sites, this geometry realized an effective one-dimensional chain with a collectively enhanced Rabi frequency $\sqrt{3}\Omega$. The average filling was 0.8 atoms/site and at the edge it dropped to below 0.1 atoms/site, within one lattice site. The coupling to the Rydberg state was realized by a two-photon process via the intermediate state $5P_{3/2}$, using laser wavelengths of 780 nm and 480 nm with σ^- and σ^+ polarizations, respectively [26]. Detailed excitation beam parameters are summarized in Table 1. Fast control of the Rabi frequency $\Omega(t)$ and the detuning $\Delta(t)$ was implemented by tuning intensity and frequency of the 780 nm excitation laser using a calibrated acousto-optical modulator (Methods). Finally, the Rydberg atoms were detected locally by fluorescence imaging after removing the ground state atoms from the trap and de-pumping the Rydberg state back to the ground state (Methods) [26]. The spatial distribution of Rydberg atoms was measured by averaging over at least 40 realizations (Fig. 1e-f). It directly reveals the crystalline order in small one-dimensional systems, where the translational invariance is broken and all crystalline excitation patterns with $N_e > 1$ are pinned to the

boundary.

In a first series of experiments, we prepared crystalline states in the 1D geometry. For fixed system size the weak scaling of the blockade radius R_b with the detuning $R_b \propto \Delta_{\text{max}}^{-1/6}$ limits the maximal excitation number that can be realized experimentally. Hence, instead of varying the detuning, we changed the length ℓ of the initial system to explore the characteristics of the Rydberg crystals [2]. We measured the mean number of Rydberg excitations N_e for varying length ℓ using a numerically optimized sweep (Fig. 5a and Methods). In the optimization the sweep duration was set to $4 \mu\text{s}$, which is a reasonable compromise between the decreasing detection efficiency for longer sweeps and adiabaticity (Methods). The results for the sweep to $\Delta_{\text{max}} = 2\pi \cdot 700(200) \text{ kHz}$ shown in Fig. 2a exhibit clear plateaus in the mean excitation number N_e and agree well with numerical predictions which take into account the initial atomic density, the actual sweep and the detection efficiency $\alpha = 0.62(5)$ (Methods). On the plateaus the theory predicts strong overlap with Fock states (Fig. 7). Exploiting the fact that varying the detuning Δ_{max} is approximately equivalent to varying the system size ℓ (Methods), we extract the compressibility $\kappa = \frac{\partial N_e}{\partial \Delta_{\text{max}}}$ from our data. As shown in Fig. 2b, κ is found to vanish in the plateau regions, as expected for an incompressible crystalline Fock state, and in overall good agreement with our theoretical results. The finite values in between result from the small energy gaps between different Fock states around Δ_c , leading to the preparation of compressible superposition states.

The preparation involves complex quantum dynamics of the many-body system. To trace the evolution of the crystallization process along the sweep trajectory ($\Omega(t), \Delta(t)$) we abruptly switched off the coupling at

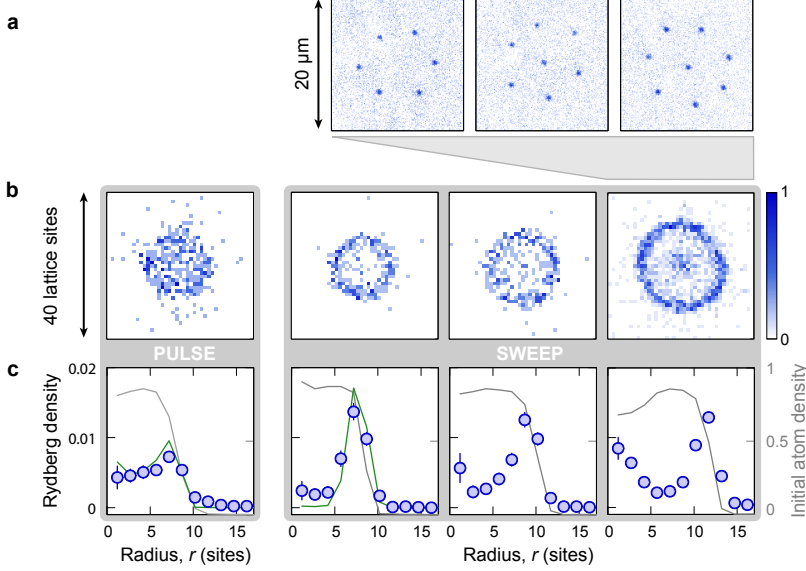


Figure 4. Dynamical crystallization in two dimensions. **a**, Unprocessed experimental single shot pictures of Rydberg states with 6, 7 and 8 excitations from the rightmost data set. Each blue point corresponds to a single atom. **b**, **c**, Rydberg densities for pulsed excitation (left grey box) and swept excitation with increasing cloud size (right grey box). The pulsed excitation was done with the same amplitude modulation as for the sweep (Fig. 5b), but the detuning Δ was held constant (averaged data for $\Delta = 2\pi \cdot 260$ kHz and $\Delta = 2\pi \cdot 760$ kHz is shown). The cloud radius was 8.2(2), 8.3(1), 10.0(3), 11.8(2) lattice sites (left to right). **b**, Measured two-dimensional distribution of Rydberg excitations. The colour scale represents the normalized counts per site. **c**, Azimuthally averaged density distribution (probability per site) of the data shown in **b** (blue dots) and comparison with theory (green line). The theoretical calculation was only feasible for small clouds and is based on representative experimental initial atomic samples. Their density is shown in grey on the right axis. Error bars s.e.m.

different times, thereby projecting the many-body state onto the eigenstates of the uncoupled system ($\Omega = 0$). For the measurement we chose the optimized sweep for the $N_e = 3$ Fock state in a system of 3×23 sites. The path through the phase diagram is shown in Fig. 3a. For each evolution time we measured the excitation number histogram, from which we extracted the mean Rydberg number $\langle \hat{N}_e \rangle$ and its normalized variance $Q = \frac{\langle \hat{N}_e^2 \rangle - \langle \hat{N}_e \rangle^2}{\langle \hat{N}_e \rangle} - 1$ (Fig. 3b). During the sweep N_e increases until we observe a saturation behaviour which we interpret as the onset of crystallization (Fig. 6). Simultaneously, the Q factor decreases from the Poissonian value $Q \approx 0$ to $Q \approx -0.5(1)$, which reflects the approach to the Fock state. The expected value $Q \approx -1$ is increased to $Q \approx -\alpha$ due to our detection efficiency. The measurement of the full counting statistics along the sweep trajectory allows for a more quantitative comparison with theory (Fig. 3c). However, the finite detection efficiency strongly affects the observed histograms and leads to a tail of the distributions towards lower excitation numbers (Methods). Nevertheless, when adapting the theoretical prediction to take $\alpha = 0.62$ into account, we find very good agreement with the experimental observations.

The high-resolution detection scheme allows for an even more detailed study of the dynamics via the spatial excitation density, which is largely unaffected by the finite detection efficiency. At the beginning of the pulse, where the excitation probability is low, we observe delocalized Rydberg atoms throughout the cloud (Fig. 3d), characteristic for the disordered phase in this parameter regime. For longer times the excitations start to accumulate at both ends of the line-shaped cloud and finally crystallize to the expected triple-peak configuration. The dynamics of this crystallization process matches well with

the theoretical expectations and the slight broadening of the observed peaks is compatible with the spatial resolution of the detection of one lattice site [26].

In a different set of experiments we investigated the chirped laser-excitation in small two-dimensional lattices. We used the spatial light modulator to prepare disc-shaped clouds with a controlled radius, whose value fluctuated by only one lattice site (Methods). Here, the dynamical preparation turned out to be more challenging, since effects of the fluctuating boundary are much more pronounced in two dimensions than in the effective one-dimensional geometry discussed above. Nevertheless, a proper frequency chirp of the excitation laser offers substantial control of the many-body dynamics and the preparation of energetically low-lying many-body states. This is demonstrated in Fig. 4 where we compare the spatial distribution of Rydberg atoms when exciting the atoms at a constant detuning to the result of a chirped excitation from $\Delta_{\min} < 0$ to Δ_{\max} (Fig. 5b). In the former case the excitations are delocalized across the atomic sample, while in the latter low energy states with localized excitations are prepared. The initial system size permits to control the excitation number and attainable spatial structures. With increasing N_e the configuration with all Rydberg excitations located along the circumference becomes energetically unfavourable compared to configurations with an extra Rydberg atom in the lattice centre. This structural change is directly visible in the spatial excitation patterns shown in Fig. 4.

In conclusion, we have prepared and studied the crystalline phase in a Rydberg lattice gas using coherent laser sweeps. This constitutes the first controlled preparation of crystalline states in neutral atom systems. Furthermore, these adiabatic preparation techniques enable the

detailed study of the underlying phase diagram, and intriguing phenomena such as the predicted two-stage melting via a floating crystal phase [6, 7]. More generally, our results pave the way towards the study of quantum correlations and dissipative quantum magnets in long-range

interacting Ising-type spin systems [33–35].

ACKNOWLEDGEMENTS

We acknowledge funding by MPG, DFG, EU (UQUAM, SIQS, ITN-COHERENCE, HAIRS, Marie Curie Fellowship to M.C.).

-
- [1] M. Saffman, T. Walker, and K. Mølmer, *Rev. Mod. Phys.* **82**, 2313 (2010).
 - [2] T. Pohl, E. Demler, and M. D. Lukin, *Phys. Rev. Lett.* **104**, 043002 (2010).
 - [3] J. Schachenmayer, I. Lesanovsky, A. Micheli, and A. J. Daley, *New J. Phys.* **12**, 103044 (2010).
 - [4] R. M. W. van Bijnen, S. Smit, K. a. H. van Leeuwen, E. J. D. Vredenbregt, and S. J. J. M. F. Kokkelmans, *J. Phys. B At. Mol. Opt. Phys.* **44**, 184008 (2011).
 - [5] H. Weimer, R. Löw, T. Pfau, and H. P. Büchler, *Phys. Rev. Lett.* **101**, 250601 (2008).
 - [6] H. Weimer and H. P. Büchler, *Phys. Rev. Lett.* **105**, 230403 (2010).
 - [7] E. Sela, M. Punk, and M. Garst, *Phys. Rev. B* **84**, 085434 (2011).
 - [8] I. Lesanovsky, *Phys. Rev. Lett.* **106**, 025301 (2011).
 - [9] R. Löw, H. Weimer, J. Nipper, J. B. Balewski, B. Butscher, H. P. Büchler, and T. Pfau, *J. Phys. B At. Mol. Opt. Phys.* **45**, 113001 (2012).
 - [10] C. S. Hofmann, G. Günter, H. Schempp, N. L. M. Müller, A. Faber, H. Busche, M. Robert-de Saint-Vincent, S. Whitlock, and M. Weidemüller, *Front. Phys.* (2013), 10.1007/s11467-013-0396-7.
 - [11] S. Ji, C. Ates, and I. Lesanovsky, *Phys. Rev. Lett.* **107**, 060406 (2011).
 - [12] D. Jaksch, J. I. Cirac, P. Zoller, R. Côté, and M. D. Lukin, *Phys. Rev. Lett.* **85**, 2208 (2000).
 - [13] M. Lukin, M. Fleischhauer, R. Cote, L. Duan, D. Jaksch, J. Cirac, and P. Zoller, *Phys. Rev. Lett.* **87**, 037901 (2001).
 - [14] I. I. Beterov, D. B. Tretyakov, V. M. Entin, E. A. Yakshina, I. I. Ryabtsev, C. McCormick, and S. Bergamini, *Phys. Rev. A* **84**, 023413 (2011).
 - [15] R. T. Brierley, C. Creatore, P. B. Littlewood, and P. R. Eastham, *Phys. Rev. Lett.* **109**, 043002 (2012).
 - [16] D. Petrosyan and K. Mølmer, *Phys. Rev. A* **87**, 033416 (2013).
 - [17] M. Ebert, A. Gill, M. Gibbons, X. Zhang, M. Saffman, and T. G. Walker, *Phys. Rev. Lett.* **112**, 043602 (2014).
 - [18] R. Löw, H. Weimer, U. Krohn, R. Heidemann, V. Bendkowsky, B. Butscher, H. Büchler, and T. Pfau, *Phys. Rev. A* **80**, 033422 (2009).
 - [19] N. Malossi, M. M. Valado, S. Scotto, P. Huillery, P. Pillet, D. Ciampini, E. Arimondo, and O. Morsch, *arXiv:1308.1854* (2013).
 - [20] H. Schempp, G. Günter, M. Robert-de Saint-Vincent, C. S. Hofmann, D. Breyel, A. Komnik, D. W. Schönleber, M. Gärttner, J. Evers, S. Whitlock, and M. Weidemüller, *Phys. Rev. Lett.* **112**, 013002 (2014).
 - [21] Y. Dudin, F. Bariani, and A. Kuzmich, *Phys. Rev. Lett.* **109**, 133602 (2012).
 - [22] T. Peyronel, O. Firstenberg, Q.-Y. Liang, S. Hofferberth, A. V. Gorshkov, T. Pohl, M. D. Lukin, and V. Vuletić, *Nature* **488**, 57 (2012).
 - [23] S. Bettelli, D. Maxwell, T. Fernholz, C. S. Adams, I. Lesanovsky, and C. Ates, *Phys. Rev. A* **88**, 043436 (2013).
 - [24] A. Schwarzkopf, R. Sapiro, and G. Raithel, *Phys. Rev. Lett.* **107**, 103001 (2011).
 - [25] M. Viteau, M. Bason, J. Radogostowicz, N. Malossi, D. Ciampini, O. Morsch, and E. Arimondo, *Phys. Rev. Lett.* **107**, 060402 (2011).
 - [26] P. Schauß, M. Cheneau, M. Endres, T. Fukuhara, S. Hild, A. Omran, T. Pohl, C. Gross, S. Kuhr, and I. Bloch, *Nature* **491**, 87 (2012).
 - [27] W. Anderson, J. Veale, and T. Gallagher, *Phys. Rev. Lett.* **80**, 249 (1998).
 - [28] I. Mourachko, D. Comparat, F. de Tomasi, A. Fioretti, P. Nosbaum, V. Akulin, and P. Pillet, *Phys. Rev. Lett.* **80**, 253 (1998).
 - [29] P. Bak and R. Bruinsma, *Phys. Rev. Lett.* **49**, 249 (1982).
 - [30] C. Ates and I. Lesanovsky, *Phys. Rev. A* **86**, 013408 (2012).
 - [31] J. F. Sherson, C. Weitenberg, M. Endres, M. Cheneau, I. Bloch, and S. Kuhr, *Nature* **467**, 68 (2010).
 - [32] T. Fukuhara, P. Schauß, M. Endres, S. Hild, M. Cheneau, I. Bloch, and C. Gross, *Nature* **502**, 76 (2013).
 - [33] I. Lesanovsky, B. Olmos, and J. Garrahan, *Phys. Rev. Lett.* **105**, 100603 (2010).
 - [34] C. Ates, B. Olmos, J. P. Garrahan, and I. Lesanovsky, *Phys. Rev. A* **85**, 043620 (2012).
 - [35] D. Petrosyan, M. Höning, and M. Fleischhauer, *Phys. Rev. A* **87**, 053414 (2013).
 - [36] M. Greiner, O. Mandel, T. Esslinger, T. W. Hänsch, and I. Bloch, *Nature* **415**, 39 (2002).
 - [37] T. Fukuhara, A. Kantian, M. Endres, M. Cheneau, P. Schauß, S. Hild, D. Bellem, U. Schollwöck, T. Giamarchi, C. Gross, I. Bloch, and S. Kuhr, *Nat. Phys.* **9**, 235 (2013).
 - [38] B. Fornberg, *Math. Comput.* **51**, 699 (1988).

METHODS

Rydberg excitation

The excitation path, detection scheme, laser setup and optical lattice configuration during the Rydberg excitation were explained in a previous publication [26]. The beam parameters are summarized in Table I.

We realized the required frequency and amplitude

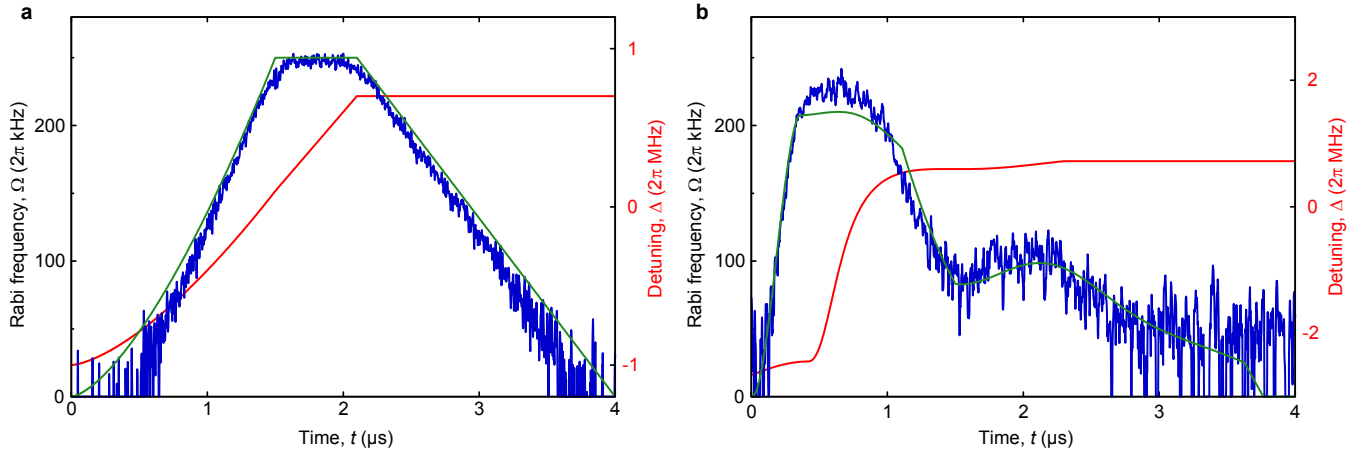


Figure 5. **Frequency and amplitude modulation of the sweeps in 1D and 2D.** Time dependence of Rabi frequency and detuning during the sweep used in the experiments with 1D systems (a) and 2D systems (b). Blue line, two-photon Rabi frequency obtained by a calibrated photo diode. The noise is due to the low light level on the high-bandwidth photo diode. For the 2D systems the pulse was not optimized using the full procedure discussed in the Methods, since the limiting factor here was the fluctuation of the cloud shape. For the largest 2D systems (Fig. 4, rightmost column) the Rabi frequency was scaled up by a factor of 1.9(1) compared to b. Green line, targeted two-photon Rabi frequency. Red line, targeted detuning.

modulation of the two-photon coupling by changing the parameters of the red beam (780 nm), while the parameters for the blue beam (480 nm) were held constant. The fast modulations were implemented using an acousto-optical modulator in double-pass configuration at a centre frequency of 350 MHz. For the frequency sweep a synthesizer with large frequency modulation bandwidth was used to drive the acousto-optical modulator. The pulse amplitude was shaped using a fast, calibrated variable attenuator after the synthesizer. Long-term drifts were minimized by a sample-and-hold intensity stabilization technique.

We measured the resonance curve of the Rydberg excitation in a very dilute cloud to avoid interaction induced broadening and shifts. Over consecutive days the line centre was reproducible within about 200 kHz. The linewidth of the Rydberg lasers was 50 kHz for the red laser and 20 kHz for the blue laser. To measure the Rabi frequency Ω of the two-photon coupling we prepared a single atom using our addressing technique and observed its Rabi oscillations.

The use of the red laser to implement the amplitude modulation lead to a time-dependent Stark shift on the ground state, which caused an additional detuning of the transition to the Rydberg state. This effect had to be compensated during the sweep, as it can easily exceed the two-photon Rabi frequency. The Stark shifts on the intermediate and Rydberg states were negligible, the former due to the vanishing influence of the level shift on the excitation scheme, the latter due to the weak coupling. The amplitude and frequency modulation throughout the sweeps are shown in Fig. 5.

The relatively small beam waist of the excitation beams (Table I) lead to a spatial variation of the Rabi

frequency Ω across the system. For most of the measurements the difference in coupling strength was less than 30 %, but for the largest one-dimensional systems with $\ell > 26$ up to 40 %.

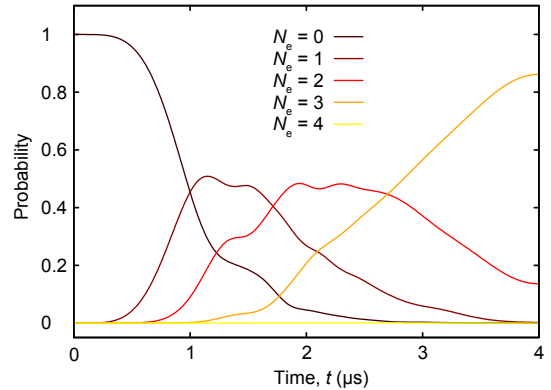


Figure 6. **Calculated time-evolution of the Rydberg Fock state population during the optimized sweep in 1D.** Calculation of the time-dependent occupation of the Fock states for an ideal 3×23 chain with unity filling.

Rydberg detection

For detection of the Rydberg atoms we removed the ground state atoms shortly after the excitation, followed by the de-excitation of the Rydberg atoms using resonant coupling to the short-lived $5P_{3/2}$ state. Finally, we detected the remaining atoms via fluorescence imaging in the optical lattice. The ground state push-out

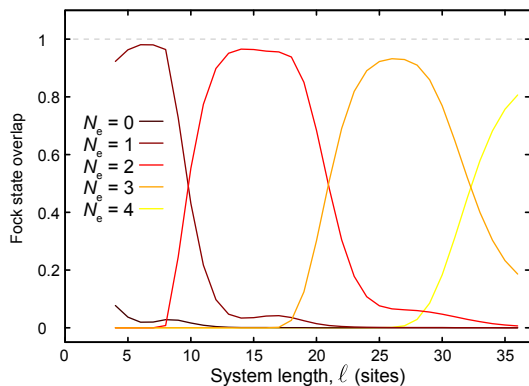


Figure 7. **Calculated dependence of the Rydberg Fock state population after the sweep on the system length.** Calculation of the Fock state overlap of the state after the sweep for a $3 \times \ell$ system taking into account length fluctuations and a filling of 0.8 atoms/site of the initial atom configurations.

had to be as short as possible, to allow for high detection efficiency and high spatial resolution. At the same time a very high pushing efficiency was required. We optimized the ground state removal under these restrictions to a short pulse of $6 \mu\text{s}$ in total. A re-pumping laser on the $5S_{1/2}$, $|F, m_F\rangle = |1, -1\rangle \leftrightarrow 5P_{3/2}$, $|2, -2\rangle$ transition was switched on for the full $6 \mu\text{s}$ while the push beam ($5S_{1/2}$, $|2, -2\rangle \leftrightarrow 5P_{3/2}$, $|3, -3\rangle$) was delayed by $2 \mu\text{s}$. The Rabi frequencies on both transitions were approximately $2\pi \cdot 70 \text{ MHz}$. We used a relatively high re-pump power to include also the other Zeeman sub-states of the $5S_{1/2}$, $|F = 1\rangle$ manifold, which were split by $\Delta m_F \cdot 21 \text{ MHz}$ for our magnetic field of 30 G. The re-pump beam is required to remove the very small fraction of atoms in $|F = 1\rangle$ states, created by imperfect state preparation, scattering of the red Rydberg beam and non-perfect polarization of the push-beam. This scheme allows to reach a push-out efficiency of 99.9% within the limited time.

Limits for the detection efficiency

Our detection method allows for high-resolution imaging of the Rydberg atoms. However, this requires fast de-pumping of the Rydberg atoms into the ground state. Initially the ground state atoms were prepared in the lowest band of the optical lattice. The excitation to the slightly anti-trapped Rydberg state caused an expansion of the centre of mass wave function during the push-out time. The instantaneous de-pumping to the ground state then lead to a projection of the expanded and, due to the Rydberg-Rydberg interaction, slightly shifted wave function onto the lattice eigenstates, such that several bands

in the lattice were populated. Before switching on the optical molasses for the fluorescence imaging we had to wait for 57 ms to make sure that the absolute value of the magnetic field is below 100 mG, which is required for the molasses to work properly. During this time, the population in higher bands tunnelled through the lattice. Most of these atoms were not detected and the rest caused a flat background in the images.

The detection efficiency of $\alpha = 0.62(5)$ is determined from the data shown in Fig. 2a. The determined value is consistent with independent measurements in Fig. 3c and Fig. 4.

Initial atomic sample preparation

After cooling the rubidium-87 atoms the experiment began with a 2D-Bose-Einstein condensate in the hyperfine state $|1, -1\rangle$ trapped in the vertical lattice. We used a de-confining beam at 670 nm to reduce the radial trap frequencies. To reduce interferences on this beam, it was generated using a super-luminescent diode (linewidth $\approx 5 \text{ nm}$) and then amplified in two consecutive tapered amplifiers.

Next, we adiabatically switched on the horizontal lattices and created an atomic Mott-insulator [36]. We made sure that the centre of the system was in the unity filling Mott lobe by adjusting the atom number. This allowed to create unity filling regions of a diameter of up to $15 \mu\text{m}$. Only for very large systems (c.f. Fig. 2a, $\ell > 27$ and Fig. 4c, rightmost panel) we had to allow for double occupancy in the central part.

A spatial light modulator was used to project a line- or disc-shaped pattern with adjustable size onto the atoms [37]. Intensity, polarization and detuning of this light pattern were chosen to create a differential light shift on the transition $|1, -1\rangle \leftrightarrow |2, -2\rangle$ of approximately 50 kHz, but nearly no absolute shift of the $|1, -1\rangle$ state. Next, the atoms on non-shifted sites were transferred to the $|2, -2\rangle$ state using a microwave sweep and subsequently removed by resonant laser light on the $5S_{1/2}$, $|2, -2\rangle \leftrightarrow 5P_{3/2}$, $|3, -3\rangle$ transition. The final step was to transfer the remaining atoms via a microwave sweep to the $|2, -2\rangle$ state. The average filling in the remaining part of the system was 0.8 atoms/site.

Numerical pulse optimization

Our theoretical calculations are based on a numerical solution of the Schrödinger equation for the Hamiltonian (1) in a truncated Hilbert space. To this end, we expand the wave function $|\psi\rangle$ of the N_{at} -atom system in terms of Fock-states, which are eigenstates of the classical Hamiltonian (i.e. for $\Omega = 0$)

$$|\psi\rangle = c^{(0)}|0\rangle + \sum_{\mathbf{i}_1} c_{\mathbf{i}_1}^{(1)}|\mathbf{i}_1\rangle + \sum_{\mathbf{i}_1, \mathbf{i}_2} c_{\mathbf{i}_1, \mathbf{i}_2}^{(2)}|\mathbf{i}_1, \mathbf{i}_2\rangle + \dots + \sum_{\mathbf{i}_1, \dots, \mathbf{i}_{N_{\text{at}}}} c_{\mathbf{i}_1, \dots, \mathbf{i}_{N_{\text{at}}}}^{(N_{\text{at}})}|\mathbf{i}_1, \dots, \mathbf{i}_{N_{\text{at}}}\rangle, \quad (2)$$

where $|\mathbf{i}_1, \dots, \mathbf{i}_N\rangle$ corresponds to a state with N Rydberg excitations located at lattice sites \mathbf{i}_1 to \mathbf{i}_N , and $c_{\mathbf{i}_1, \dots, \mathbf{i}_N}^{(N)}$ denotes the corresponding time-dependent amplitude. In order to truncate the otherwise exponentially large Hilbert space we only include excitation numbers of $N \leq N_c$ and introduce a cut-off distance R_c , discarding all states that contain Rydberg excitations closer than R_c [26]. The presented results were obtained for $N_c = 5$ and we verified directly that the inclusion of states with $N = 6, 7$ did not contribute to the many-body dynamics. In addition R_c was reduced progressively until convergence of the simulated dynamics was achieved [26].

In order to optimize the excitation pulse we monitor the fidelity

$$\mathcal{F}(|\psi(t)\rangle, |\psi_{\text{GS}}(t)\rangle) = |\langle\psi_{\text{GS}}(t)|\psi(t)\rangle|^2, \quad (3)$$

i.e., the overlap between the time-evolving wave function $|\psi(t)\rangle$ and the many-body ground state $|\psi_{\text{GS}}(t)\rangle$ at time t determined by the actual set of laser parameters $\Omega(t)$ and $\Delta(t)$. First we choose a given trajectory $(\Omega(t), \Delta(t))$ that connects the initial ground state with all atoms de-excited with the targeted crystalline ground state. The actual path chosen for our experiments is shown in Fig. 3a. Next we discretize the path into a large number of sampling points, forming equal linear segments, along which we propagate the Schrödinger equation as described above. A suitable pulse for high-fidelity Fock-state generation was then obtained by optimizing the local ramp speed for each segment with respect to the decrease of $\mathcal{F}(t)$ between successive sampling points, with the constraint $T = 4\mu\text{s}$ for the total pulse duration, T .

As described in the main text, non-adiabatic transitions between closely lying states with equal N but finite displacements are unavoidable in the final stage of the excitation pulse. Hence, for the chosen path, we stop the optimization and fixed the ramp speed once the Rabi frequency drops below 60 kHz. Since the experimentally prepared atomic lattice has a finite filling fraction of ≈ 0.8 , this procedure is repeated for several random configurations producing slightly different optimal pulses. The pulse shown in Figure 5a was constructed as a simple and simultaneously good compromise between those numerically obtained pulses for $\ell = 23$. As demonstrated in Fig. 7, this pulse indeed yields a high final Fock-state fidelity of 0.98, 0.96 and 0.93 for $N_e = 1$, $N_e = 2$ and $N_e = 3$ excitations, respectively. In our experiments, this pulse was used to obtain the Rydberg blockade staircase shown in Fig. 2.

Estimating the compressibility

In the dilute limit, $N_e \ll \ell$, the Hamiltonian Eq. (1) for a 1D chain can be reformulated in a continuous form. To this end, we scale lengths and energies by $L = \ell a_{\text{lat}}$ and C_6/L^6 , and introduce dimensionless operators

$$\begin{aligned} \hat{\psi}(x_i) &= \sqrt{\frac{L}{a_{\text{lat}}}} |g^{(i)}\rangle \langle e^{(i)}| = \sqrt{\ell} |g^{(i)}\rangle \langle e^{(i)}|, \\ \hat{\psi}^\dagger(x_i) &= \sqrt{\ell} |e^{(i)}\rangle \langle g^{(i)}|, \end{aligned} \quad (4)$$

where $x_i = i a_{\text{lat}}/L$. Taking the continuum limit, this permits to write the lattice Hamiltonian as

$$\hat{H} = B_\perp \int_0^1 (\hat{\psi}^\dagger(x) + \hat{\psi}(x)) dx + B_\parallel \int_0^1 \hat{\psi}^\dagger(x) \hat{\psi}(x) dx + \frac{1}{2} \iint_0^1 \frac{\hat{\psi}^\dagger(x) \hat{\psi}^\dagger(x') \hat{\psi}(x') \hat{\psi}(x)}{|x - x'|^6} dx dx' \quad (5)$$

with the dimensionless, effective magnetic fields $B_\perp = \sqrt{\ell} \frac{\hbar \Omega}{2} \frac{L^6}{C_6}$ and $B_\parallel = -\hbar \Delta \frac{L^6}{C_6}$. The quantum fields $\hat{\psi}^\dagger$ and $\hat{\psi}$ describe the creation and annihilation of hard-core bosons, where the hard-core constraint is naturally ensured by the Rydberg-Rydberg atom interaction. The excitation number, and, hence, the density increases linearly with L , such that $L \rightarrow \infty$ defines the thermodynamic limit.

Consequently the excitation number $N_e = N_e(B_\parallel, B_\perp)$ depends on only two parameters and we can re-express the compressibility $\kappa = \frac{\partial N_e}{\partial \Delta}$ in terms of the derivative of N_e with respect to ℓ . Neglecting the weak dependence

on B_\perp , thus, yields

$$\kappa = \frac{\ell}{6\Delta} \frac{\partial N_e}{\partial \ell}, \quad (6)$$

which we used to calculate the compressibility κ from the measured dipole-blockade staircase shown in Fig. 2. The required ℓ -derivative was obtained from the experimental data, $N_e^{(i)}$ and $\ell^{(i)}$, by using a second-order symmetric formula [38]: $\frac{\partial N_e}{\partial \ell} \big|_{\ell=\bar{\ell}^{(i)}} \approx \frac{N_e^{(i+1)} - N_e^{(i-1)}}{\ell^{(i+1)} - \ell^{(i-1)}}$ with $\bar{\ell}^{(i)} = \frac{1}{2}(\ell^{(i+1)} + \ell^{(i-1)})$.

In order to verify the quality of the employed approximations, we also determined κ numerically directly from

		red pulse 1D	red pulse 2D	blue
max. Rabi freq 2photon	$(2\pi \cdot \text{kHz})$	250(25)	420(42)	-
max. Rabi frequency	$(2\pi \cdot \text{MHz})$	29(2)	49(3)	13(2)
max. Intensity	(mW/cm^2)	76(5)	215(14)	$1.4(3) \times 10^6$
beam waist	(μm)	44(2)	44(2)	17(5)
max. light shift	$(2\pi \cdot \text{kHz})$	236(35)	670(100)	57(9)

Table I. **Parameters of the Rydberg laser beams.** For the red laser in the 1D configuration (first column), and 2D (second column). The blue laser (third column) has the same parameters in 1D and 2D. Errors, s.d.

its definition. To this end, we recorded the excitation number staircase using the excitation pulse $(\Omega(t), \Delta(t))$ shown in the Figure 5a and for a reference pulse with a small global frequency shift δ , i.e. for $(\Omega(t), \Delta(t) + \delta)$. Within the studied range $|\delta/(2\pi)| < 10 \text{ kHz}$ the num-

ber of excitations N_e was found to vary linearly with δ such that the compressibility can be evaluated directly via $\kappa = (N_e(\delta) - N_e(\delta = 0))/\delta$. This compressibility κ is shown in Fig. 2b and agrees well with the experimental results obtained from equation (6).